A&A 648, A118 (2021)
https://doi.org/10.1051/0004-6361/202140385

Astronomy & Astrophysics

Observations of 12.2 GHz methanol masers towards northern high-mass protostellar objects

M. Durjasz, M. Szymczak, P. Wolak, and A. Bartkiewicz

Institute of Astronomy, Faculty of Physics, Astronomy and Informatics, Nicolaus Copernicus University, Grudziadzka 5, 87-100 Torun, Poland
e-mail: md@astro.umk.pl

Received 20 January 2021 / Accepted 12 March 2021

ABSTRACT

Context. Class II methanol masers at 6.7 and 12.2 GHz occur close to high-mass young stellar objects (HMYSOs). When they are observed simultaneously, such studies may contribute to refining the characterisation of local physical conditions.
Aims. We aim to search for the 12.2 GHz methanol emission in 6.7 GHz methanol masers that might have gone undetected in previous surveys of northern sky HMYSOs, mainly due to their variability. Contemporaneous observations of both transitions are used to refine the flux density ratio and examine the physical parameters.
Methods. We observed a sample of 153 sites of 6.7 GHz methanol maser emission in the 12.2 GHz methanol line with the Torun 32 m radio telescope, using the newly built *X*-band receiver.
Results. The 12.2 GHz methanol maser emission was detected in 36 HMYSOs, with 4 of them detected for the first time. The 6.7–12.2 GHz flux density ratio for spectral features of the contemporaneously observed sources has a median value of 5.1, which is in agreement with earlier reports. The ratio differs significantly among the sources and for the periodic source G107.298+5.639 specifically, the ratio is weakly recurrent from cycle to cycle, but it generally reaches a minimum around the flare peak. This is consistent with the stochastic maser process, where small variations in the physical parameters along the maser path can significantly affect the ratio. A comparison of our data with historical results (from about ten years ago) implies significant (>50%) variability for about 47 and 14% at 12.2 and 6.7 GHz, respectively. This difference can be explained via the standard model of methanol masers.

Key words. masers – stars: massive – stars: formation – ISM: molecules – radio lines: ISM

1. Introduction

Masers play a significant role in the study of the interstellar medium. The methanol molecule has attracted much attention, from its first detection half a century ago (Barrett et al. 1971) to the present, given the multitude of observed transitions. One of the breakthroughs in the field came with the detection of the strongest, and most pervasive, lines at 12.2 (Batrla et al. 1987) and 6.7 GHz (Menten 1991), which provided powerful tools for identifying high-mass young stellar objects (HMYSOs) and exploring the physical conditions and gas kinematics of their surroundings. A number of new methanol transitions in the centimetre (Breen et al. 2019; MacLeod et al. 2019) and millimetre (Brogan et al. 2019) ranges have been discovered very recently in objects that have undergone major accretion events.

The 6.7 and 12.2 GHz lines are referred to as class II methanol maser transitions (Batrla et al. 1987; Menten 1991) that are characterised by radiative pumping (Cragg et al. 2005) and a close association with sources of strong radiation. They are usually found in the vicinity of HYMSOs, as revealed by several surveys at 6.7 GHz (e.g. Caswell et al. 1995b; Ellingsen et al. 1996; Pandian et al. 2007; Szymczak et al. 2012; Green et al. 2010; Breen et al. 2015). Several searches for the 12.2 GHz methanol maser emission were carried out prior to the discovery of the 6.7 GHz line, mainly towards OH maser sites (Norris et al. 1987; Koo et al. 1988; Kemball et al. 1988; Caswell et al. 1993; MacLeod et al. 1993). Thereafter, all the 12.2 GHz surveys were done towards the 6.7 GHz sources (Gaylard et al. 1994; Caswell et al. 1995a; Błaszkiewicz & Kus 2004; Breen et al. 2010, 2012a,b, 2014, 2015), as the 12.2 GHz line excitation conditions closely follow those at 6.7 GHz (Cragg et al. 2002). Almost all of these surveys did not cover the entire northern sky, thus, in this study, we attempt to supplement the observations with objects of the northern hemisphere.

No conclusive data is available on the variability patterns of the 12.2 GHz methanol masers. Little or no variability was noticed on a timescale of seven months in eight bright (>100 Jy) 12.2 GHz maser sources (McCutcheon et al. 1988), whereas in the other five bright sources, the emission varied internally by less than 15–20% over a four-year period with the exception of single weak features in two sources (MacLeod et al. 1993). In turn, Caswell et al. (1993) reported the 12.2 GHz flux density variations on a timescale of weeks and later found that at least a quarter of the features exhibit intensity variations larger than 10% on a timescale of 4 yr (Caswell et al. 1995a) suggesting that most quiescent 12.2 GHz masers are saturated. In this paper, we present the results of multi-epoch 12.2 GHz observations, along with a comparison to historical observations, for 153 sources. We include several contemporaneously monitored 6.7 GHz methanol maser counterparts.

2. Observations

Observations were carried out in the period from 2019 August to 2020 February using the Torun 32 m radio telescope. The telescope has a half-power beam width of about 3′ at 12.2 GHz and

rms pointing errors of about 10″. The adopted rest frequency was 12.178597 GHz (Müller et al. 2004). We used the newly built *X*-band receiver (Pazderski 2018), which is a dual-polarisation cooled receiver with amplifiers of typical noise temperature of 5 K. Here, the system temperature was about 30 K. The antenna gain was estimated to be about 0.06 K Jy^{-1} from observations of calibrators DR21 and 3C123 adopting flux densities of 20.0 and 6.3 Jy, respectively (Ott et al. 1994). No gain elevation correction was applied; this can contribute less than 4% to the error budget of the flux density. The uncertainty in the flux density scale is about 15%.

The observations were made in frequency-switching mode. An autocorrelation spectrometer was configured to record 4096 channels either with 4 MHz or 8 MHz bandwidth for each circularly polarised signal yielding the channel spacing of 0.024 or 0.048 km s^{-1}, respectively. The velocity extent of each observation is ±45 or ±90 km s^{-1} with respect to the local standard of rest. A typical 3σ noise level in the final spectra with the higher spectral resolution was 1.5 Jy. The stability of the system was regularly checked with observations of G188.946+0.886 that show no variability to a limit of 15% during our observing interval, while its 12.2 GHz spectrum shape remained almost unchanged after $\gtrsim$10 yr when observed by Breen et al. (2012a). Observations of G188.946+0.886 during the 2000–2008 revealed periodic (395±8 d) variability with relative amplitudes of 0.5 and 0.7 at 6.7 and 12.2 GHz, respectively, but periodic changes at 12.2 GHz were barely visible prior to 2005 (Goedhart et al. 2014, their Figs. 9 and 10). In the period from 2009 to 2013, the relative amplitude of periodic variations at 6.7 GHz decreased to about 0.2 (Szymczak et al. 2018), whereas our unpublished 6.7 GHz observations, carried out contemporaneously with the present 12.2 GHz survey, show a variability that is lower than 10% We argue that the variability of this object at 12 GHz does not exceed the uncertainty of our measurements. For selected sources, contemporaneous (≤±7 d) observations were carried out in the 6.7 GHz methanol transition following the procedure described in Szymczak et al. (2018).

We selected bright 6.7 GHz sources (Breen et al. 2015; Szymczak et al. 2012; Hu et al. 2016; Green et al. 2010) that are observable from the northern hemisphere and mostly with a declination of >0° to avoid a degradation of the telescope sensitivity due to radio frequency interference from commercial satellites. The final sample consists of 153 sources.

3. Results

The 12.2 GHz maser emission was detected in 36 objects (Table 1), including four new sources. Figures 1 and A.1 present the spectra of newly detected and previously known sources, respectively. The list of non-detections is also given in Table A.1.

3.1. Newly detected 12.2 GHz sources

G50.035+0.582. This source has a single 12.2 GHz feature at −5.1 km s^{-1}, with $S_{12.2}$ = 1.1 Jy, which coincides with the strongest feature of the 6.7 GHz methanol maser (Szymczak et al. 2012; Breen et al. 2015). There was no 12.2 GHz maser emission detected in 2010 March with the 5σ sensitivity of 0.84 Jy (Breen et al. 2016). This implies a variability of ≥30% on a timescale of 9.5 yr.

G85.410+0.003. The 12.2 GHz spectrum is comprised of three features at −31.5, −29.5, and −28.6 km s^{-1}. These are coincident with their 6.7 GHz maser counterparts, within 0.1 km s^{-1},

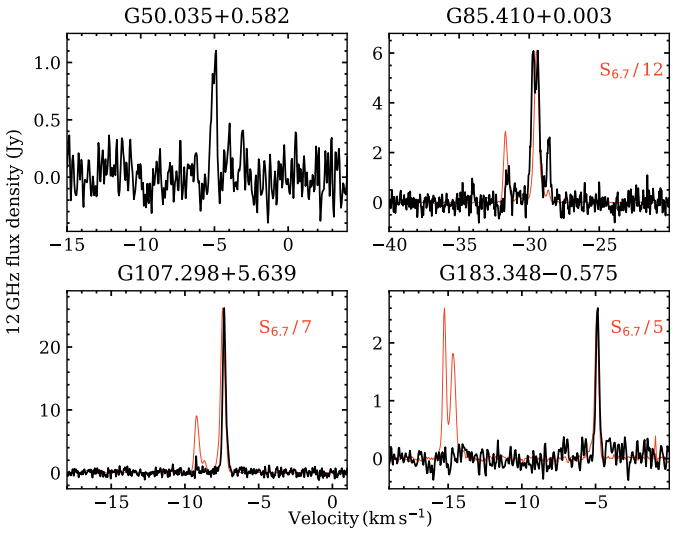

Fig. 1. Spectra of the newly detected 12.2 GHz methanol maser sources. Spectra of 6.7 GHz methanol masers (red) are also shown when taken on the same day, with exception of G183.348−0.575, where the interval between observations was 41 d. For comparison purposes, the scale of 6.7 GHz flux density was reduced by the factor given in the upper right corner.

observed in the same epoch. In instances where a single bright feature at $V_{12.2}$ = −29.5 km s^{-1} was originally detected, we now report two features separated by 0.3 km s^{-1}. A comparison with the Effelsberg 100 m spectrum taken on May 19, 2020 (Yen & Menten, priv. comm. at M2O[1]) implies significant changes in the profile shape and flux density of individual features by a factor of 2–3 over four months.

G107.298+5.639. The single velocity feature is matched in velocity to the strongest 6.7 GHz feature at −7.35 km s^{-1} (Olech et al. 2020) during all three observed cycles, which are discussed in detail in Sect. 3.2. Hereafter, G107.298+5.639 is referred to as G107.

G183.348−0.575. The 12.2 GHz maser emission consists of a single feature at −4.9 km s^{-1} with a peak flux density of 2.5 Jy, which coincides in velocity with the 6.7 GHz maser feature. There was no 12.2 GHz maser emission seen for the blueshifted component of the 6.7 GHz emission near −15 km s^{-1}.

3.2. Case of G107

The 12.2 GHz maser emission follows periodic variations observed in the methanol 6.7 GHz and hydroxyl (1.665/1.667 GHz) maser lines (Szymczak et al. 2016; Olech et al. 2020). The upper panel in Fig. 2 presents the light curves of both methanol transitions. In order to estimate the parameters of flare profiles, we fitted an asymmetric power function (David et al. 1996; Szymczak et al. 2011), Gaussian function, and second-order polynomial to the 6.7 and 12.2 GHz data. The flare maximum and timescale of variability FWHM of the flare are listed in Table 2 for each transition and three cycles. For the asymmetric function fitting we get, in addition, the ratio of rise to decay time of the flare, which ranges from 0.8 to 1.1 and 0.7 to 0.9 for the 12.2 and 6.7 GHz lines, respectively. This suggests that the flare profile at 12.2 GHz is slightly more symmetric than the one at 6.7 GHz. The full width at half maximum (FWHM)

[1] https://www.masermonitoring.com

Table 1. Detected 12.2 GHz methanol maser sources.

Name (l b) (° °)	α (J2000) (h m s)	δ (J2000) (° ′ ″)	$V_{\rm peak}$ (km s^{-1})	$S_{\rm peak}$ (Jy)	ΔV (km s^{-1})	$S_{\rm int}$ (Jy km s^{-1})	Epoch (MJD)	References
G30.225−0.180	18 47 08.30	−02 29 28.90	113.35	6.7	107;116	8.76	58 723	9,11
G32.744−0.075	18 51 21.87	−00 12 05.00	30.55	3.7	29;40	5.81	58 769	6,9,11,14
G33.641−0.228	18 53 32.56	00 31 39.18	60.26	37.8	58;62	13.13	58 868	11,14
G35.132−0.744	18 58 06.14	01 37 07.50	29.72	11.8	27;32	10.83	58 872	14
G35.197−0.743	18 58 13.05	01 40 35.70	28.26	39.1	27;32	31.7	58 873	6,7,9,11,14
G35.200−1.736	19 01 45.54	01 13 32.60	45.16	11.9	43;47	4.23	58 873	2,4,5,6,9,10,11,14
G36.115+0.552	18 55 16.79	03 05 05.41	75.08	2.4	73;78	1.32	58 720	14
G37.043−0.035	18 59 04.41	03 38 32.80	83.88	3.0	83;85	0.85	58 880	14
G37.430+1.518	18 54 14.23	04 41 41.10	41.32	73.8	40;43	31.79	58 862	8,11,14
G37.546−0.112	19 00 16.05	04 03 16.09	50.03	1.1	49;51	0.58	58 866	14
G40.282−0.219	19 05 41.21	06 26 12.69	74.35	1.7	72;81	2.61	58 716	14
G40.425+0.700	19 02 39.62	06 59 10.50	6.62	7.9	5;16	5.60	58 827	14
G42.034+0.190	19 07 28.18	08 10 53.47	11.50	4.6	10;15	6.09	58 872	14
G43.149+0.013	19 10 11.05	09 05 20.40	13.64	2.4	13;15	0.94	58 766	1,9,11,14
G43.890−0.784	19 14 26.39	09 22 36.50	51.66	2.4	45;53	1.71	58 805	11,14
G45.804−0.356	19 16 31.08	11 16 12.01	60.01	1.3	59;61	0.18	58 762	14
G49.043−1.079	19 25 22.25	13 47 19.50	36.31	0.9	35;37	0.49	58 721	14
G49.265+0.311	19 20 44.85	14 38 26.91	−4.55	1.4	−7;−3	1.83	58 827	14
G49.349+0.413	19 20 32.44	14 45 45.44	68.14	2.0	66;70	1.24	58 860	14
G49.416+0.326	19 20 59.21	14 46 49.60	−10.18	0.8	−10.8;−9.5	0.45	58 726	11,14
G49.489−0.369	19 23 39.82	14 31 04.90	59.01	2.3	57;60	1.37	58 855	14
G49.490−0.388	19 23 43.95	14 30 34.20	56.13	10.1	55;57	5.30	58 855	1,5,6,9,11,12,14
G49.599−0.249	19 23 26.61	14 40 16.99	64.05	4.3	61;67	9.97	58 706	11,14
G50.035+0.582 [(a)]	19 21 15.45	15 26 49.20	−5.02	1.1	−6;−3	0.41	58 717	
G52.199+0.723	19 24 59.84	17 25 17.90	3.31	2.8	2;5	1.01	58 760	14
G52.663−1.092	19 32 36.07	16 57 38.40	65.22	2.6	64;67	1.24	58 870	11,14
G59.783+0.065	19 43 11.25	23 44 03.30	26.96	4.3	26;29	1.97	58 870	9,11
G79.736+0.991	20 30 50.67	41 02 27.60	−5.59	4.7	−7;−4	3.04	58 713	11
G85.410+0.003 [(a)]	20 54 13.68	44 54 07.60	−29.74	5.7	−33;−27	5.63	58 870	
G107.298+5.639 [(a)]	22 21 22.50	63 51 13.00	−7.34	25.1	−9;−6	8.44	58 677	
G109.871+2.114	22 56 17.90	62 01 49.65	−4.07	44.5	−5;−1	10.99	58 902	4,5,11
G111.542+0.777	23 13 45.36	61 28 10.55	−61.30	36.7	−55;−62	49.46	58 702	1,4,5,11
G133.947+1.064	02 27 03.82	61 52 25.40	−44.54	601.3	−47;−41	1334.22	58 770	1,4,5,11
G183.348−0.575 [(a)]	05 51 10.94	25 46 17.24	−4.87	2.6	−6;−4	1.15	58 703	
G188.946+0.886	06 08 53.34	21 38 29.16	10.84	268.0	8;12	196.28	58 892	3,4,5,6,9,11,13
G192.600−0.048	06 12 54.02	17 59 23.32	5.84	25.9	3;7	17.40	58 723	12,13

Notes. Column 1 presents the methanol maser galactic coordinates, Cols. 2–3 give equatorial coordinates of the 6.7 GHz methanol masers (Breen et al. 2016; Szymczak et al. 2012; Hu et al. 2016). Columns 4–8 present characteristics of the obtained spectra; the velocity of the strongest peak relative to the local standard of rest ($V_{\rm peak}$), peak flux density ($S_{\rm peak}$), velocity range of the maser emission (ΔV), integrated flux density ($S_{\rm int}$), and epoch of observation, respectively. For G107.298+5.639 the epoch of the strongest flare was selected. The last column list the references to previous detections. [(a)]Newly detected 12.2 GHz maser.

References. (1) Batrla et al. (1987); (2) Norris et al. (1987); (3) Kemball et al. (1988); (4) Koo et al. (1988); (5) Catarzi et al. (1993); (6) Caswell et al. (1993); (7) MacLeod et al. (1993); (8) Gaylard et al. (1994); (9) Caswell et al. (1995a); (10) Moscadelli & Catarzi (1996); (11) Błaszkiewicz & Kus (2004); (12) Breen et al. (2010); (13) Breen et al. (2012a); (14) Breen et al. (2016).

values of 12.2 GHz flares (1.8−4.5 d) vary from cycle to cycle much more than those of 6.7 GHz flares (4.4−5.8 d), suggesting a greater variability of the 12.2 GHz emission.

There is a systematic delay between 6.7 and 12.2 GHz flare peaks (Table 2) for each of the three cycles (lower panel in Fig. 2). The average delay obtained from the results of the three fits is 0.9±0.3 d. The VLBI maps indicate that the 6.7 GHz emission near −7.35 km s^{-1} comes from clouds located ∼150 au from the putative position of the central star (Olech et al. 2020). Thus, if the 6.7 and 12.2 GHz maser coexist, then the observed delay cannot be explained by a simple geometrical effect. We may speculate that the actual size of the region conducive for 6.7 GHz maser emission is more extended than it would be for 12.2 GHz maser emission and both maser regions may not coincide precisely. Further interferometric studies are needed to verify this possibility.

The lower part of Fig. 2 shows variations in the 6.7 to 12.2 GHz flux density ratio ($R_{6/12}$) over the cycles. There are significant differences in the temporal behaviour of $R_{6/12}$ over the flare profile from cycle to cycle. For the best sampled observations of the second cycle, with a peak around MJD 58 714, $R_{6/12}$ falls from 22 at flare onset to 10.4 at flare maximum and then increases to 32 as the flare decays. The average value of $R_{6/12}$ for the three cycles around the flare peaks is 8.1 which is very close to the median ratio reported in Caswell et al. (1995b) and Breen et al. (2014).

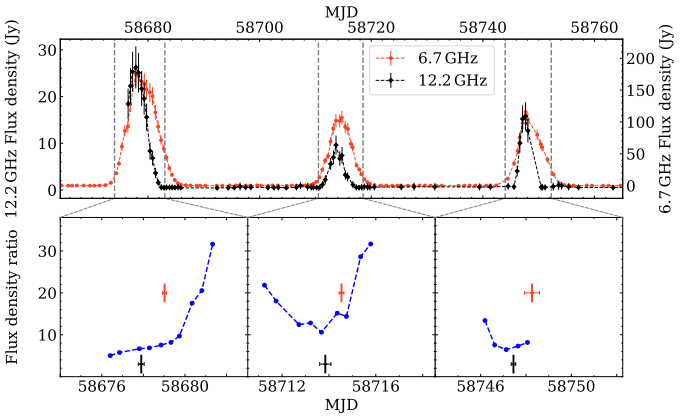

Fig. 2. Light curves of the −7.4 km s^{-1} methanol maser feature at 12.2 (black) and 6.7 GHz (red) for G107.298+5.639 (*upper panel*). Temporal changes in the 6.7–12.2 GHz flux density ratio are plotted (blue) (*lower panel*). The thick vertical error bars denote the flare maxima at 12.2 (black) and 6.7 GHz (red) calculated as the average value of the peak times obtained with the use of three methods (Table 2), whereas the thin horizontal error bars mark the corresponding standard errors.

Table 2. Flare parameters retrieved from the three model fitting.

6.7 GHz			12.2 GHz		
Epoch (MJD)	*FWHM* (d)	S_p (Jy)	Epoch (MJD)	*FWHM* (d)	S_p (Jy)
Asymmetric power function					
58 678.80	5.76	175.5	58 677.85	4.46	26.0
58 714.46	4.41	107.6	58 713.82	2.90	8.4
58 748.20	4.52	112.0	58 747.43	1.93	16.5
Gaussian function					
58 679.25	5.18	191.4	58 677.93	3.81	27.2
58 714.63	4.37	109.5	58 713.82	2.85	8.4
58 748.59	4.53	113.4	58 747.46	1.81	16.9
2-nd order polynomial					
58 679.02	–	162.6	58 677.91	–	25.6
58 714.51	–	99.5	58 713.90	–	8.1
58 748.00	–	110.2	58 747.45	–	16.2

Notes. The points with the flux density greater than 50% of the peak value were used for the parabola fitting. S_p is the fitted flux density at flare peak.

4. Comments on previously known sources

In this section, we provide commentary on our observational data with the aim of providing useful information on the 6.7 to 12.2 GHz flux density ratio. Taken together with results of previous surveys given in Table 1, it is possible to estimate the degree and timescale of variability.

G30.225−0.180. The 12.2 GHz maser spectrum detected in September and December 1992 by Caswell et al. (1995a) was composed of two features at $V_{12.2}$ = 112.8 and 113.6 km s^{-1}, with a peak flux density $S_{12.2}$ ∼ 2.8 and 1.2 Jy, respectively. Our observations reveal the spectrum of different shape with a peak flux density of $S_{12.2}$ = 6.7 Jy at $V_{12.2}$ = 113.3 km s^{-1}. There was no emission found, with a 5σ sensitivity level of 1.8 Jy, in March 2010 (Breen et al. 2016). This implies significant variability on timescales of 9–27 yr. The emission at a velocity lower than 111 km s^{-1} (Fig. A.1) comes from another source, namely, G30.198−0.169 (Caswell et al. 1995a; Breen et al. 2016), which was detected in the beam sidelobe.

G32.744−0.075. A comparison of our observations with those in the literature suggests that the overall spectral profile of the 12.2 GHz maser emission has been unchanged over more than 40 yr (Caswell et al. 1993). The peak flux density of individual features differ by ≤40% on timescales of 9–27 yr (Caswell et al. 1993, 1995a; Breen et al. 2016), suggesting only modest variability.

G33.641−0.228. The brightest features in our spectrum have similar velocities to those reported in Breen et al. (2016), but their flux densities differ by a factor of 0.3–2.3. Furthermore, the emission at $V_{12.2}$ = 58.8 km s^{-1} decreased by an order of magnitude as compared to that observed in 2002 by Błaszkiewicz & Kus (2004). This implies significant variability on timescales of 9–18 yr. The source also shows a variety of variability patterns in the 6.7 GHz methanol maser emission from short (2–5 d) flares, with a seven-fold rise within 24 hr (Fujisawa et al. 2012, 2014), up to quasi-periodic (>500 d) variations of low amplitude (Olech et al. 2019).

G35.132−0.744. The strongest feature at $V_{12.2}$ = 31.2 km s^{-1} that was observed by Breen et al. (2016) increased by a factor of 2, whereas the feature at $V_{12.2}$ = 29.7 km s^{-1} increased by one order of magnitude. This implies strong variability on a timescale of 9 yr.

G35.197−0.743. The spectrum observed in April 1988 (Caswell et al. 1993) is complex, with a prominent feature at $V_{12.2}$ = 30.5 km s^{-1}, with a peak flux of $S_{12.2}$ = 44 Jy. The intensity of this feature decreased by ∼30%, while the emission peak at $V_{12.2}$ = 28.5 km s^{-1} increased by the same amount after ∼4.5 yr (Caswell et al. 1995a). MacLeod et al. (1993) and Błaszkiewicz & Kus (2004) reported the spectrum similar to that observed in December 1992 by Caswell et al. (1995a), while the Breen et al. (2016) spectrum is similar to that presented in Caswell et al. (1993). Thus, from the data reported in the literature we infer a variability of 30–40% on a timescale of 4–20 yr. Our survey suggests that this level of variability remains on timescale of ≥30 yr for the redshifted emission (30.5 km s^{-1}) but the feature at $V_{12.2}$ = 28.2 km s^{-1} increased by a factor of 4 as compared to the spectrum from Breen et al. (2016).

G35.200−1.736. Norris et al. (1987) reported the spectrum, consisting of two features at $V_{12.2}$ = 41.5 and 45.0 km s^{-1} with peak flux densities of $S_{12.2}$ = 100 and 146 Jy, respectively. A similar spectrum was seen after 1–5 yr with slight (≤15%) decreases of peak intensity (Caswell et al. 1993, 1995a; Catarzi et al. 1993). Observations in 2002 (Błaszkiewicz & Kus 2004) and 2010 (Breen et al. 2016) displayed an ongoing complex spectrum with two prominent features but with the flux density of the strongest feature at $V_{12.2}$ = 45.0 km s^{-1} decreasing to $S_{12.2}$ = ∼80 Jy in 2002 and $S_{12.2}$ = 46 Jy in 2010. We report only a single feature with a peak of $S_{12.2}$ = 12 Jy at $V_{12.2}$ = 45.2 km s^{-1}. We conclude that the 12.2 GHz line intensity declined by an order of magnitude within 32 yr.

G37.430+1.518. Our spectrum, with a single feature of $S_{12.2}$ = 74 Jy at $V_{12.2}$ = 41.3 km s^{-1}, is very similar to that reported by Błaszkiewicz & Kus (2004) and Breen et al. (2016), implying a variability lower than 20% on a timescale of 17 yr. The

emission observed 26 yr ago (Gaylard et al. 1994) was a factor of 6 weaker, suggesting significant variability on longer timescales.

G40.282−0.219. The three-feature spectrum is similar to that observed nine years ago (Breen et al. 2016) but the flux density of the primary feature at $V_{12.2}$ = 74.3 km s^{-1} decreased by ∼50%.

G42.034+0.190. We detected a weak and complex 12.2 GHz spectrum of similar shape to that shown in Breen et al. (2016). In general, the intensity of features increased by a factor of 1.8–4.5 after nine years.

G43.149+0.013. The 12.2 GHz spectrum consisted of a single feature at $V_{12.2}$ = 13.6 km s^{-1}. Its intensity declined by 35% over 26 yr (Caswell et al. 1995a; Breen et al. 2016).

G43.890−0.784. Little variability is visible in the two features at $V_{12.2}$ = 47.4 and 51.8 km s^{-1} when compared to spectra from 2002 (Błaszkiewicz & Kus 2004) an 2010 (Breen et al. 2016). From our observations, it can be seen that the emission at $V_{12.2}$ = 51.8 km s^{-1} decreased by a factor of 2. There was no emission detected at $V_{12.2}$ = 47.7 km s^{-1}, whereas a new feature appeared at $V_{12.2}$ = 45.3 km s^{-1}, indicating significant variability.

G49.043−1.079. Nine years ago, this 12.2 GHz source had a complex spectra (Breen et al. 2016). In our observations, the strongest feature they detected ($S_{12.2}$ = 7.1 Jy at $V_{12.2}$ = 37.4 km s^{-1}) is now only ∼1 Jy. This suggests strong variability on this timescale.

G49.416+0.326. The spectrum is similar to that presented in Breen et al. (2016), with little variability above the noise level.

G49.490−0.388. The spectrum is composed of the emission from G49.489−0.369 and G49.490−0.388 as part of the W51 complex. Batrla et al. (1987) discovered a single feature, with a peak flux density of $S_{12.2}$ = 8 Jy at $V_{12.2}$ ∼ 56 km s^{-1}, and a broad absorption feature (from 60 to 75 km s^{-1}). Catarzi et al. (1993) observed a similar spectrum with a peak flux density of $S_{12.2}$ = 20 Jy without absorption. Caswell et al. (1993, 1995a) also reported one feature with the peak flux density of $S_{12.2}$ = 14 and 21 Jy, respectively with barely visible absorption. A simple spectrum with a single feature at $V_{12.2}$ = 56.2 km s^{-1} with $S_{12.2}$ = 13.8 Jy was also observed by Błaszkiewicz & Kus (2004). The flux density of this feature dropped to 4.5–5.5 Jy (in 2008 and 2010, Breen et al. 2016) and increased to ∼10 Jy during our observations. This suggests that the emission towards G49.490−0.388 shows significant and complicated temporal changes. Features at velocity >56.6 km s^{-1} were also visible only in 2010 (Breen et al. 2016) that might suggest variability of G49.489−0.369. It is difficult, given our beam size, to distinguish unequivocally which spectral feature comes from which object; hence, the velocity ranges marked in Fig. A.1 are taken from Breen et al. (2016).

G49.599−0.249. The spectrum is almost the same as the one seen in Breen et al. (2016), with the exception of the 63.0 km s^{-1} feature, which decreased by a factor of 2 after 9 yr.

G59.783+0.065. The feature at $V_{12.2}$ = 27.1 km s^{-1} declined from $S_{12.2}$ = 15.8 Jy in 1992 (Caswell et al. 1995a) to $S_{12.2}$ = 9.2 Jy in 2002 (Błaszkiewicz & Kus 2004) and $S_{12.2}$ = 4.3 Jy during our observations. The second feature at $V_{12.2}$ = 17.0 km s^{-1}, with a peak flux of $S_{12.2}$ = 4 Jy (Caswell et al. 1995a) increased by ∼50% (Błaszkiewicz & Kus 2004) and decreased below our sensitivity limit of ∼1 Jy.

G109.871+2.114. Observations made in 1990 (Catarzi et al. 1993), with a peak flux density of $S_{12.2}$ = 128.8 Jy at $V_{12.2}$ = −4.15 km s^{-1}, found a similar spectral profile shape to that seen in 1987 (Koo et al. 1988), but with flux density that was a factor of ∼2 lower. Błaszkiewicz & Kus (2004) revealed a similar profile but with peak flux densities that were a factor of 3 lower than Koo et al. (1988). We detected a complex spectrum with the emission from $V_{12.2}$ = −5 to −1 km s^{-1} and a peak flux density of $S_{12.2}$ = 45 Jy at $V_{12.2}$ = −4.1 km s^{-1}. Thus, the source is significantly variable, namely, by a factor of 7 on a timescale of ∼30 yr.

G111.542+0.777. Batrla et al. (1987) discovered a double peaked spectrum, the brightest feature at $V_{12.2}$ = −56.3 km s^{-1}, with $S_{12.2}$ ∼200 Jy remained stable within 15% over 1–3 yr (Koo et al. 1988; Catarzi et al. 1993). The spectral shape was found to be unchanged in 2002 (Błaszkiewicz & Kus 2004) but the peak flux density decreased by a factor of 2. Here, we present a very different spectrum with several blended features from −62 to −55 km s^{-1}. The feature at $V_{12.2}$ = −56.3 km s^{-1} dimmed by a factor of 20 compared to that reported by Batrla et al. (1987), whereas the feature near $V_{12.2}$ = −61.5 km s^{-1} increased by a factor of less than 2. This suggests strong variability on a timescale of ≥20 yr.

G188.946+0.886. The flux density of the strongest feature at $V_{12.2}$ = 10.4 km s^{-1} increased by ∼30% between 1987 and 1992 (Koo et al. 1988; Kemball et al. 1988; Caswell et al. 1993, 1995a; Catarzi et al. 1993). The profile of the spectrum significantly transformed in 2008 (Breen et al. 2012a) but the intensity remained unchanged within 10%. We found spectra similar to those reported in Breen et al. (2012a), and the peak flux of feature at $V_{12.2}$ = 10.8 km s^{-1} increased by ∼15%. More information on the variability of this object is provided in Sect. 2.

G192.600−0.048. A faint (0.5–0.6 Jy) feature at $V_{12.2}$ = 3.6 km s^{-1} was detected in June and December 2008 (Breen et al. 2012a). Our observations revealed a complex spectrum with the strongest feature of $S_{12.2}$ = 26 Jy at $V_{12.2}$ = 5.8 km s^{-1}. Significant change in the spectral profile and intensity is likely related to a significant outburst of a 6.7 GHz maser that occurred in mid-2015 (Moscadelli et al. 2017; Szymczak et al. 2018).

There is a group of 12.2 GHz masers that have gone undetected in the present survey (Table A.1) and 13 out of those 17 masers were observed with a 5σ sensitivity of 0.7–4.2 Jy, that is, lower than the peak flux densities at the time of their detection from the literature. We failed to detect, with 5σ sensitivity of 0.6–0.9 Jy, the following objects: G42.698−0.147, G45.467+0.053, G94.602−1.796, and G196.454−1.677, with a peak flux density of 1.2–12.3 Jy in earlier observations (Caswell et al. 1995a; Błaszkiewicz & Kus 2004; Breen et al. 2012a, 2016). These four sources may be variable on timescales smaller than 9–28 yr.

5. Discussion

5.1. Detection rate

The present observations of our sample of 153 6.7 GHz masers resulted in the detection of 36 12.2 GHz methanol maser sources, corresponding to a ∼24% detection rate. This is about a factor of 2 lower than the overall detection rate of 43% in the Galactic longitude range of 290° ≤ l ≤ 60° (Breen et al. 2016). We compared our detection rate with the rates from Breen et al. (2016) as a function of 10° longitude bins. For the 30°−40°, 40°−50°, and

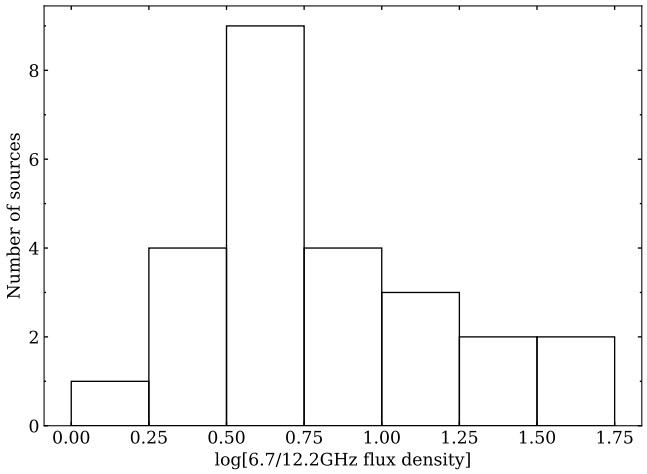

Fig. 3. Histogram of the 6.7–12.2 GHz peak flux density ratio.

50°−60° longitude bins, our detection rates are lower by 20, 9, and 2%, respectively, than those reported in Breen et al. (2016). This confirms a significant lowering of our sensitivity for low declination sources as shown in Table A.1. The reason for this is a degradation of sensitivity due to interference from geostationary satellites or imperfect removal of some corrupted scans during the edition of spectra. The detection rate in the range of $70° \leq l \leq 90°$ decreases to ∼16% and shows a statistically significant difference from that for the neighbouring range of 50°−60° (23.5%).

5.2. Flux density ratio

Our survey indicates that the flux density of individual features and integrated flux density of the 6.7 GHz maser sources are all greater than those of their 12.2 GHz counterparts. This is consistent with conclusions inferred from more comprehensive statistical analysis based on a large sample (Breen et al. 2011). In the following, we confine discussion to the flux density ratio $R_{6/12}$ for the spectral features with the same velocity in both transitions contemporaneously observed in order to exclude the possible effect of variability. There is strong observational evidence of spatial coincidence of the 6.7 and 12.2 GHz masers to within a few milliarcseconds, especially when the spectral profiles of both transitions are similar (Menten et al. 1992; Norris et al. 1993; Minier et al. 2000; Moscadelli et al. 2002). Thus, it is suggestive that the flux density comparison can be meaningful in the absence of high angular resolution maps. We found 70% of the detected 12.2 GHz methanol maser peaks are coincident in velocity with the 6.7 GHz maser peak.

For the 6.7 and 12.2 GHz spectra of nine sources taken within 7 days of each other, we performed Gaussian function fits to obtain the velocity and flux density of feature peaks. For all features with the same peak velocity (±0.1 km s^{-1}) at both transitions, the flux density ratio, $R_{6/12}$, was determined (Table 3). The range of $R_{6/12}$ is 1.5 to 50.9, with a median value of 5.1 (Fig. 3). Our median is comparable to that determined by Caswell et al. (1995b). The analysis by Breen et al. (2011) of the statistical properties of 580 southern sources found a median peak-to-peak ratio of 4.3. Although their samples are more numerous, with little overlap with ours, the median ratios are similar. This suggests that each of these samples come from a similar population of HMYSOs.

There is a significant dispersion of $R_{6/12}$ for spectral features of some sources (e.g. G111.524+0.777, Table 3). Furthermore, our observations of G107 reveal that around the flare maxima, $R_{6/12}$ varies by up to 50% between two consecutive cycles. In addition, the temporal behaviour of $R_{6/12}$ is poorly repeated from cycle to cycle, even though a general trend remains, that is, the ratio reaches a minimum around the flare peak and is larger at the onset and final stages of the flare profile. This could be caused by variations in the physical conditions along the maser path length of 10^{16} cm (Moscadelli et al. 2002) for individual features on different timescales.

In G107, the maser intensity varies with a period of 34.4 days, perhaps due to changes of infrared emission (Olech et al. 2020); it is difficult to identify processes that can significantly change the gas density, molecule abundance, and kinetic temperature in the maser regions on such a short timescale. Since the heating and cooling times of dust grains are less than a few minutes and one day, respectively, for the optically thick case (van der Walt et al. 2009; Johnstone et al. 2013), rapid changes in the maser intensity may be related to variations in the dust temperature (T_d). Timescales of gas heating and cooling are 2–3 orders of magnitude greater than those of dust grains (e.g. Johnstone et al. 2013); thus, the gas temperature variation can affect the maser emission in G107 on timescales of several months.

Numerical models of infrared pumping indicate that the 6.7 and 12.2 GHz methanol masers over a wide range of the gas densities and kinetic temperatures (Cragg et al. 2002, 2005), but there is a narrow range of dust temperature, T_d, for which the flux ratio varies quite rapidly (Cragg et al. 2005, their Fig. 2). When the dust temperature increases from ∼130 to ∼170 K, $R_{6/12}$ decreases by a factor of 2 and vice versa. Therefore, the variations in T_d qualitatively explain the observed change in the flux ratio during the flare of G107. However, it should be noted that the temporal behaviour of $R_{6/12}$ varies considerably from cycle to cycle, which is possibly the result of small variations in the physical conditions along the maser path and the degree of saturation (e.g. Breen et al. 2012b). High-cadence monitoring observations combined with a high angular resolution are required to resolve this discrepancy.

5.3. Variability

There are 24 detected sources in our sample that are in common with those observed by Breen et al. (2016) at 12.2 GHz and Breen et al. (2015) at 6.7 GHz, providing an opportunity to study variations on a timescale of ∼10 yr. Seven objects with spectra comprised of multiple sources were not considered. In Fig. 4, we present the relative changes in the integrated flux density (S_{int}) between the two methanol maser transitions. In Fig. 5, the same analysis is presented, but for peak flux densities (Table A.2 shows exact values). Among 17 sources detected in two epochs, only two show S_{int} variability of more than 50% in both transitions, these are: G35.200−1.736 and G49.043−1.079. The first object dimmed by a factor of 14.5 and 8.2 at 12.2 GHz and 6.7 GHz, respectively. The second object weakened by a factor of 12.7 at 12.2 GHz but only a factor of 2.3 at 6.7 GHz. G36.115+0.552 decreased by a factor of 2.2 at both lines. Two other objects (G45.804−0.356 and G49.265+0.311) varied by slightly more than 50% at 12.2 GHz but did not show significant variability at 6.7 GHz. For the subsample of 17 sources, the median value of relative changes in S_{int} is 1.19 and 1.33 for the 6.7 and 12.2 GHz lines, respectively. This general trend of a larger level of variability at 12.2 GHz than that at 6.7 GHz is more pronounced for the entire sample (Figs. 4 and 5) and is consistent with the standard model of methanol masers (Cragg et al. 2002, 2005). They demonstrated that both masers operate in a wide range of gas

Table 3. 6.7–12.2 GHz flux density ratio ($R_{6/12}$) for the Gaussian fitted features for all the sources contemporaneously observed at both maser transitions.

Source (l b) (° °)	V (km s^{-1})	$S_{6.7}$ (Jy)	$S_{12.2}$ (Jy)	$R_{6/12}$
G35.200−1.736	44.62	34.3(0.4)	2.1(0.4)	16.0(2.4)
	45.21	17.8(0.2)	11.9(0.3)	1.5(0.1)
G49.416+0.326	−10.13	2.3(0.1)	0.8(0.2)	2.7(0.6)
G49.599−0.249	65.51	10.5(2.0)	3.0(0.6)	3.5(1.0)
	62.93	15.9(0.1)	3.7(0.1)	4.3(0.1)
	64.14	15.4(0.3)	4.5(0.2)	3.4(0.2)
	64.61	16.6(2.3)	4.2(0.2)	3.9(0.6)
	65.34	15.3(4.0)	3.0(0.6)	5.1(1.7)
G85.410+0.003	−31.55	9.9(3.5)	1.2(0.2)	8.4(3.1)
	−28.65	5.7(0.2)	2.5(0.2)	2.3(0.2)
G107.29+5.64	−7.35	170.2(1.0)	25.8(0.4)	6.6(0.2)
G109.871+2.114	−3.72	125.7(22.0)	3.8(0.2)	32.7(5.9)
	−1.80	245.8(1.4)	4.8(0.2)	50.9(1.6)
G111.542+0.777	−61.33	154.9(0.6)	36.7(0.4)	4.2(0.1)
	−60.77	118.7(0.5)	14.6(0.3)	8.1(0.2)
	−58.08	230.2(3.2)	12.0(0.3)	19.2(0.6)
	−57.60	151.2(3.5)	7.0(0.8)	21.6(2.3)
	−57.22	91.7(6.0)	6.6(0.5)	13.9(1.3)
	−56.75	93.9(0.7)	13.4(0.3)	7.0(0.2)
G188.946+0.886	10.43	400.4(3.9)	109.2(3.2)	3.7(0.2)
	10.86	858.2(4.7)	269.6(1.8)	3.2(0.1)
G192.600−0.048	3.93	8.8(0.4)	4.0(0.2)	2.2(0.2)
	4.79	13.5(0.4)	5.3(0.3)	2.5(0.2)
	5.46	55.6(1.4)	5.2(0.5)	10.7(1.0)
	5.83	139.7(3.3)	25.5(0.5)	5.5(0.2)

Notes. The fitted peak velocity (V), peak flux density at 6.7 ($S_{6.7}$) and at 12.2 GHz ($S_{12.2}$) are listed. The values in brackets correspond to uncertainty, derived from covariance matrix of the least-squares fit method.

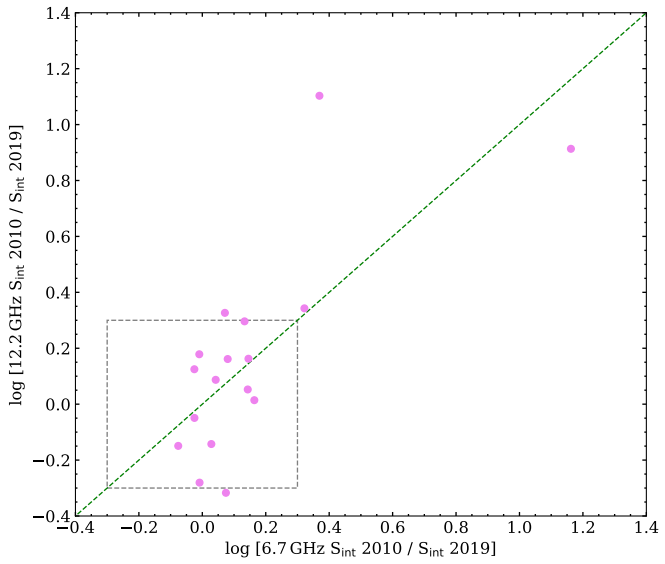

Fig. 4. Relative change in the integrated flux density, $S_{\rm int}$ at 6.7 and 12.2 GHz between 2010 (Breen et al. 2015, 2016) and 2019 (this survey). The square marks 50% level of variability.

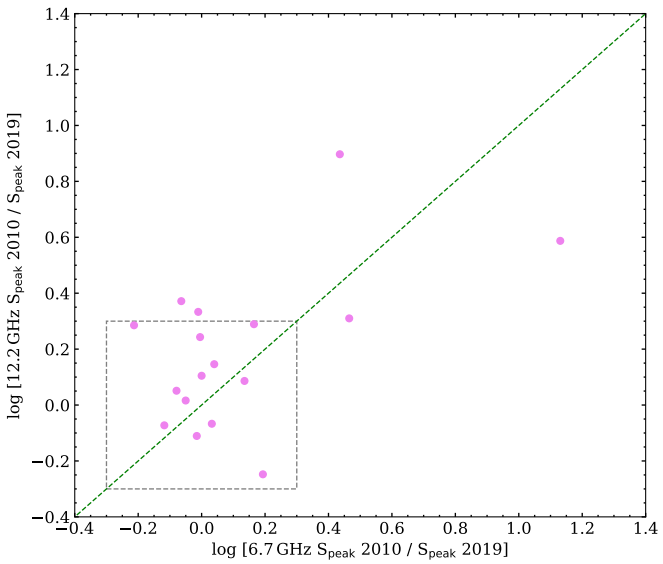

Fig. 5. Relative change in the peak flux density, $S_{\rm peak}$ at 6.7 and 12.2 GHz between 2010 (Breen et al. 2015, 2016) and 2019 (this survey). The square marks 50% level of variability. Data used to create this graph is presented in Table A.2.

density (10^4–10^8 cm^{-3}), gas temperature (30–200 K), and dust temperature (130–350 K) but we can see that the slopes of the intensity versus these parameters are more flat at 6.7 GHz than at 12.2 GHz (Cragg et al. 2005). Thus, long-term (9–10 yr) changes of the parameters may lead to higher variability in the 12.2 GHz line. Since high angular resolution interferometric studies have revealed that the 6.7 and 12.2 GHz emission is spatially coincident, the effect of turbulence or changes in velocity coherence

should be the same for both transitions. Table A.2 also presents comparison of the number of the features visible in 12.2 GHz spectra among the literature data (Breen et al. 2016) and this survey. Many of the features generally remain unchanged (±1 feature), with the exception of G35.200−1.736, for which a significant decrease of luminosity is observed in both 6.7 and 12.2 GHz lines.

6. Conclusions

We report that we detected 36 12.2 GHz methanol masers in our sample of 153, of which 4 are new detections, corresponding to detection rate of 24%.

Values of the 6.7–12.2 GHz flux density ratio for spectral features at the same velocity, when both transitions are observed contemporaneously, are within the range from 1.5 to 51. The median value of 5.1 is similar to that reported for other large samples of HYMSOs. This ratio in the periodic source G107.298+5.639 is smallest when the flare reaches its maximum, but it varies considerably from cycle to cycle. It decreases from its maximum value at the onset through its minimum at the peak of the flare and then increases during the decay phase of the flare. This temporal behaviour appears to be consistent with the standard model of methanol masers when the dust temperature varies in the narrow range of 130–170 K.

A minority (14%) of the objects that we observed show strong (>50%) variability at 6.7 GHz over a timescale of 9–10 yr, but at 12.2 GHz, nearly half of the observed sources experienced strong variability. These results appear to be compatible with maser model predictions.

Acknowledgements. We thank the staff of the 32 m telescope for assistance with the observations. We also thank the referee for the careful reading of the manuscript and recommendations. The research has made use of the SIMBAD data base, operated at CDS (Strasbourg, France), as well as NASA's Astrophysics Data System Bibliographic Services. The 32 m telescope is operated by the Institute of Astronomy, Nicolaus Copernicus University and supported by the Polish Ministry of Science and Higher Education SpUB grant.

References

Barrett, A. H., Schwartz, P. R., & Waters, J. W. 1971, ApJ, 168, L101
Batrla, W., Matthews, H. E., Menten, K. M., & Walmsley, C. M. 1987, Nature, 326, 49
Błaszkiewicz, L., & Kus, A. J. 2004, A&A, 413, 233
Breen, S. L., Ellingsen, S. P., Caswell, J. L., & Lewis, B. E. 2010, MNRAS, 401, 2219
Breen, S. L., Ellingsen, S. P., Caswell, J. L., et al. 2011, ApJ, 733, 80
Breen, S. L., Ellingsen, S. P., Caswell, J. L., et al. 2012a, MNRAS, 426, 2189
Breen, S. L., Ellingsen, S. P., Caswell, J. L., et al. 2012b, MNRAS, 421, 1703
Breen, S. L., Ellingsen, S. P., Caswell, J. L., et al. 2014, MNRAS, 438, 3368
Breen, S. L., Fuller, G. A., Caswell, J. L., et al. 2015, MNRAS, 450, 4109
Breen, S. L., Ellingsen, S. P., Caswell, J. L., et al. 2016, MNRAS, 459, 4066
Breen, S. L., Sobolev, A. M., Kaczmarek, J. F., et al. 2019, ApJ, 876, L25
Brogan, C. L., Hunter, T. R., Towner, A. P. M., et al. 2019, ApJ, 881, L39
Caswell, J. L., Gardner, F. F., Norris, R. P., et al. 1993, MNRAS, 260, 425
Caswell, J. L., Vaile, R. A., Ellingsen, S. P., & Norris, R. P. 1995a, MNRAS, 274, 1126
Caswell, J. L., Vaile, R. A., Ellingsen, S. P., Whiteoak, J. B., & Norris, R. P. 1995b, MNRAS, 272, 96
Catarzi, M., Moscadelli, L., & Panella, D. 1993, A&AS, 98, 127
Cragg, D. M., Sobolev, A. M., & Godfrey, P. D. 2002, MNRAS, 331, 521
Cragg, D. M., Sobolev, A. M., & Godfrey, P. D. 2005, MNRAS, 360, 533
David, P., Etoka, S., & Le Squeren, A. M. 1996, A&AS, 115, 387
Ellingsen, S. P., von Bibra, M. L., McCulloch, P. M., et al. 1996, MNRAS, 280, 378
Fujisawa, K., Sugiyama, K., Aoki, N., et al. 2012, PASJ, 64, 17
Fujisawa, K., Aoki, N., Nagadomi, Y., et al. 2014, PASJ, 66, 109
Gaylard, M. J., MacLeod, G. C., & van der Walt, D. J. 1994, MNRAS, 269, 257
Goedhart, S., Maswanganye, J. P., Gaylard, M. J., & van der Walt, D. J. 2014, MNRAS, 437, 1808
Green, J. A., Caswell, J. L., Fuller, G. A., et al. 2010, MNRAS, 409, 913
Hu, B., Menten, K. M., Wu, Y., et al. 2016, ApJ, 833, 18
Johnstone, D., Hendricks, B., Herczeg, G. J., & Bruderer, S. 2013, ApJ, 765, 133
Kemball, A. J., Gaylard, M. J., & Nicolson, G. D. 1988, ApJ, 331, L37
Koo, B.-C., Williams, D. R. D., Heiles, C., & Backer, D. C. 1988, ApJ, 326, 931
MacLeod, G. C., Gaylard, M. J., & Kemball, A. J. 1993, MNRAS, 262, 343
MacLeod, G. C., Sugiyama, K., Hunter, T. R., et al. 2019, MNRAS, 489, 3981
McCutcheon, W. H., Wellington, K. J., Norris, R. P., et al. 1988, ApJ, 333, L79
Menten, K. M. 1991, ApJ, 380, L75
Menten, K. M., Reid, M. J., Pratap, P., Moran, J. M., & Wilson, T. L. 1992, ApJ, 401, L39
Minier, V., Booth, R. S., & Conway, J. E. 2000, A&A, 362, 1093
Moscadelli, L., & Catarzi, M. 1996, A&AS, 116, 211
Moscadelli, L., Menten, K. M., Walmsley, C. M., & Reid, M. J. 2002, ApJ, 564, 813
Moscadelli, L., Sanna, A., Goddi, C., et al. 2017, A&A, 600, L8
Müller, H. S. P., Menten, K. M., & Mäder, H. 2004, A&A, 428, 1019
Norris, R. P., Caswell, J. L., Gardner, F. F., & Wellington, K. J. 1987, ApJ, 321, L159
Norris, R. P., Whiteoak, J. B., Caswell, J. L., Wieringa, M. H., & Gough, R. G. 1993, ApJ, 412, 222
Olech, M., Szymczak, M., Wolak, P., Sarniak, R., & Bartkiewicz, A. 2019, MNRAS, 486, 1236
Olech, M., Szymczak, M., Wolak, P., Gérard, E., & Bartkiewicz, A. 2020, A&A, 634, A41
Ott, M., Witzel, A., Quirrenbach, A., et al. 1994, A&A, 284, 331
Pandian, J. D., Goldsmith, P. F., & Deshpande, A. A. 2007, ApJ, 656, 255
Pazderski, E. 2018, Balt. URSI Symp., 33
Szymczak, M., Wolak, P., Bartkiewicz, A., & van Langevelde, H. J. 2011, A&A, 531, L3
Szymczak, M., Wolak, P., Bartkiewicz, A., & Borkowski, K. M. 2012, Astron. Nachr., 333, 634
Szymczak, M., Olech, M., Wolak, P., Bartkiewicz, A., & Gawroński, M. 2016, MNRAS, 459, L56
Szymczak, M., Olech, M., Sarniak, R., Wolak, P., & Bartkiewicz, A. 2018, MNRAS, 474, 219
van der Walt, D. J., Goedhart, S., & Gaylard, M. J. 2009, MNRAS, 398, 961

Appendix A: Additional material

Table A.1. Targets towards which no 12.2 GHz emission was detected in the survey.

Name (l b) (° °)	RA(J2000) (h m s)	Dec(J2000) (° ′ ″)	5σ Jy	Epoch MJD	References
G32.105−0.074	18 50 11.58	−00 46 12.32	3.00	58 827	
G33.133−0.092	18 52 07.82	00 08 12.80	3.80	58 812	1, 3, 4
G33.199+0.001	18 51 55.34	00 14 19.38	4.90	58 716	
G33.204−0.010	18 51 58.14	00 14 13.61	3.65	58 813	
G33.317−0.360	18 53 25.30	00 10 43.90	4.20	58 861	4
G33.393+0.010	18 52 14.62	00 24 52.90	3.00	58 866	4
G33.725−0.120	18 53 18.78	00 39 05.00	4.85	58 874	
G33.980−0.019	18 53 25.01	00 55 25.98	1.25	58 812	
G34.096+0.018	18 53 29.94	01 02 39.40	4.30	58 831	
G34.244+0.133	18 53 21.44	01 13 44.40	2.45	58 859	1, 3, 4
G34.257+0.153	18 53 18.63	01 14 57.40	6.80	58 866	1, 4
G34.267−0.210	18 54 37.25	01 05 33.70	2.75	58 856	
G34.396+0.222	18 53 19.08	01 24 13.80	4.15	58 860	
G34.411+0.235	18 53 17.99	01 25 25.26	3.00	58 713	
G34.751−0.093	18 55 05.22	01 34 36.26	1.95	58 860	
G34.757+0.025	18 54 40.74	01 38 06.40	2.30	58 864	
G34.822+0.352	18 53 37.84	01 50 33.00	3.20	58 875	
G35.025+0.350	18 54 00.66	02 01 19.30	2.35	58 725	3, 4
G35.226−0.354	18 56 53.15	01 52 46.89	1.75	58 706	
G35.247−0.237	18 56 30.38	01 57 08.88	3.55	58 819	
G35.397+0.025	18 55 50.78	02 12 19.10	1.85	58 868	
G35.417−0.284	18 56 59.02	02 04 55.65	2.00	58 868	
G35.457−0.179	18 56 40.98	02 09 57.16	2.75	58 875	
G35.588+0.060	18 56 04.22	02 23 28.30	5.00	58 880	
G35.793−0.175	18 57 16.89	02 27 57.91	1.70	58 882	4
G36.705+0.096	18 57 59.12	03 24 06.11	2.10	58 883	
G36.918+0.483	18 56 59.78	03 46 03.60	1.50	58 884	
G37.030−0.039	18 59 03.64	03 37 45.09	4.35	58 894	
G37.554+0.201	18 59 09.98	04 12 15.54	2.75	58 874	
G37.598+0.425	18 58 26.79	04 20 45.46	2.35	58 867	
G37.735−0.112	19 00 36.84	04 13 20.00	2.05	58 859	
G37.753−0.189	19 00 55.42	04 12 12.56	1.00	58 802	
G37.767−0.214	19 01 02.27	04 12 16.60	1.55	58 731	
G38.038−0.300	19 01 50.46	04 24 18.96	1.80	58 882	
G38.119−0.229	19 01 44.15	04 30 37.42	4.25	58 873	4
G38.203−0.067	19 01 18.73	04 39 34.29	1.95	58 856	
G38.255−0.200	19 01 52.95	04 38 39.47	1.15	58 762	
G38.258−0.073	19 01 26.25	04 42 19.90	1.80	58 867	
G38.565+0.538	18 59 49.13	05 15 28.90	1.05	58 810	
G38.598−0.212	19 02 33.46	04 56 36.40	1.75	58 857	
G38.653+0.088	19 01 35.24	05 07 47.36	1.80	58 857	
G38.916−0.353	19 03 38.65	05 09 42.49	1.40	58 818	
G39.388−0.141	19 03 45.31	05 40 42.68	1.05	58 712	
G40.623−0.138	19 06 01.63	06 46 36.50	0.90	58 714	
G40.934−0.041	19 06 15.37	07 05 54.49	1.80	58 819	
G41.121−0.107	19 06 50.24	07 14 01.49	1.70	58 867	
G41.123−0.220	19 07 14.85	07 11 00.69	1.40	58 860	
G41.156−0.201	19 07 14.37	07 13 18.10	0.90	58 713	
G41.226−0.197	19 07 21.37	07 17 08.17	0.85	58 704	
G41.347−0.136	19 07 21.84	07 25 17.27	1.80	58 856	4
G42.13+0.52	19 06 28.90	08 25 10.00	4.05	58 705	
G42.303−0.299	19 09 43.59	08 11 41.41	1.65	58 705	
G42.435−0.260	19 09 49.85	08 19 45.40	0.85	58 705	
G42.698−0.147	19 09 55.06	08 36 53.45	0.85	58 718	4
G43.038−0.453	19 11 38.98	08 46 30.71	1.05	58 722	

Notes. The source name in bold denotes previously detected masers.
References. (1) Caswell et al. (1995a); (2) Błaszkiewicz & Kus (2004) (3) Breen et al. (2010); (4) Breen et al. (2016).

Table A.1. continued.

Source (l b) (° °)	RA(J2000) (h m s)	Dec(J2000) (° ′ ″)	5σ Jy	Epoch MJD	References
G43.074−0.077	19 10 22.05	08 58 51.49	3.50	58 832	
G43.180−0.518	19 12 09.02	08 52 14.30	0.95	58 766	
G43.796−0.127	19 11 53.97	09 35 53.50	0.95	58 726	
G44.310+0.041	19 12 15.81	10 07 53.52	1.00	58 811	
G44.644−0.516	19 14 53.76	10 10 07.69	2.55	58 832	
G45.071+0.132	19 13 22.12	10 50 53.11	1.90	58 832	
G45.380−0.594	19 16 34.14	10 47 01.60	0.85	58 770	
G45.445+0.069	19 14 18.31	11 08 59.40	0.75	58 706	
G45.467+0.053	19 14 24.15	11 09 43.00	0.85	58 711	1, 4
G45.473+0.134	19 14 07.36	11 12 16.00	0.85	58 725	
G45.493+0.126	19 14 11.35	11 13 06.20	1.50	58 866	
G46.066+0.220	19 14 56.07	11 46 12.98	0.70	58 814	
G46.115+0.387	19 14 25.52	11 53 25.99	0.70	58 703	
G48.902−0.273	19 22 10.33	14 02 43.51	0.95	58 719	
G48.990−0.299	19 22 26.13	14 06 39.78	0.80	58 767	4
G49.417+0.324	19 20 59.82	14 46 49.10	0.75	58 726	
G49.470−0.371	19 23 37.90	14 29 59.30	0.95	58 810	3, 4
G49.617−0.360	19 23 52.81	14 38 03.30	1.65	58 832	
G50.315+0.676	19 21 27.47	15 44 18.60	0.75	58 802	
G50.779+0.152	19 24 17.41	15 54 01.60	1.75	58 862	4
G51.679+0.719	19 23 58.87	16 57 41.80	1.50	58 833	
G51.818+1.250	19 22 17.95	17 20 06.50	0.75	58 770	
G52.922+0.414	19 27 34.96	17 54 38.14	1.70	58 759	
G53.036+0.113	19 28 55.49	17 52 03.11	1.05	58 731	
G53.142+0.071	19 29 17.58	17 56 23.21	0.70	58 713	
G53.618+0.036	19 30 23.01	18 20 26.68	0.70	58 704	
G56.963−0.235	19 38 17.10	21 08 05.40	0.75	58 707	
G57.610+0.025	19 38 40.74	21 49 32.70	0.75	58 719	
G58.775+0.644	19 38 49.13	23 08 40.20	0.80	58 720	
G59.634−0.192	19 43 50.00	23 28 38.80	0.70	58 712	
G59.833+0.672	19 40 59.33	24 04 46.50	0.85	58 714	
G60.575+0.186	19 45 52.48	24 17 42.99	0.70	58 706	
G69.539+0.975	20 10 09.07	31 31 34.86	0.70	58 704	
G70.181+1.741	20 00 54.16	33 31 30.88	0.70	58 705	
G71.522+0.385	20 12 57.91	33 30 26.95	0.75	58 725	
G73.06+1.80	20 08 10.20	35 59 23.70	0.65	58 705	
G75.782+0.342	20 21 44.05	37 26 36.91	0.70	58 706	
G78.122+3.633	20 14 26.04	41 13 33.39	0.70	58 705	
G78.886+0.708	20 29 24.94	40 11 19.28	1.40	58 866	
G80.861+0.383	20 37 00.96	41 34 55.70	0.80	58 705	
G81.722+0.571	20 39 01.05	42 22 49.18	0.80	58 726	
G81.744+0.590	20 39 00.38	42 24 36.91	0.90	58 707	
G81.752+0.590	20 39 01.99	42 24 59.08	0.80	58 725	
G81.871+0.780	20 38 36.42	42 37 34.56	0.65	58 704	
G90.921+1.486	21 09 12.98	50 01 03.56	0.75	58 703	
G94.602−1.796	21 39 58.26	50 14 20.96	0.60	58 703	2
G97.52+3.17	21 32 13.00	55 52 56.00	0.85	58 707	
G98.035+1.446	21 43 01.43	54 56 17.75	0.75	58 712	
G108.184+5.519	22 28 51.40	64 13 41.31	0.65	58 706	
G108.766−0.986	22 58 51.18	58 45 14.37	0.95	58 702	
G111.255−0.769	23 16 10.33	59 55 28.43	0.80	58 702	
G121.298+0.659	00 36 47.35	63 29 02.16	0.75	58 712	
G123.066−6.309	00 52 24.19	56 33 43.17	0.70	58 712	
G136.845+1.167	02 49 33.59	60 48 27.95	0.85	58 705	
G173.482+2.446	05 39 13.05	35 45 51.29	0.75	58 705	
G173.70+2.89	05 41 37.40	35 48 49.00	0.70	58 726	
G174.201−0.071	05 30 48.01	33 47 54.61	0.85	58 726	
G188.793+1.030	06 09 06.96	21 50 41.23	0.80	58 703	
G189.030+0.784	06 08 40.67	21 31 06.90	0.85	58 705	
G189.471−1.216	06 02 08.37	20 09 20.10	0.80	58 727	
G189.777+0.344	06 08 35.30	20 39 06.59	0.90	58 727	
G196.454−1.677	06 14 37.05	13 49 36.16	0.80	58 719	1

Table A.2. Data used to create Fig. 5.

Source (l b)	6.7 GHz		12.2 GHz					
(° °)	$S_{\text{peak 2010}}$ (Jy)	$S_{\text{peak 2019}}$ (Jy)	$S_{\text{peak 2010}}$ (Jy)	$S_{\text{peak 2019}}$ (Jy)	$V_{\text{peak 2010}}$ (km s^{-1})	$V_{\text{peak 2019}}$ (km s^{-1})	$N_{\text{feat. 2010}}$	$N_{\text{feat. 2019}}$
G32.744−0.075	56.0	38.3	7.2	3.7	30.5	30.6	3	3
G33.641−0.228	140.0	145.0	29.3	37.8	58.8	60.3	3	2
G35.200−1.736	500.0	37.0	46.0	11.9	44.6	45.2	8	1
G36.115+0.552	40.0	13.7	4.9	2.4	74.6	75.1	1	1
G37.430+1.518	400.0	293.0	90.0	73.8	41.2	41.3	1	1
G37.546−0.112	4.0	4.0	1.4	1.1	50.0	50.0	1	1
G40.282−0.219	22.0	25.5	3.7	1.7	74.3	74.4	3	3
G40.425+0.700	22.0	24.7	8.2	7.9	6.7	6.6	2	2
G42.034+0.190	22.0	14.1	2.6	4.6	11.5	11.5	4	4
G43.890−0.784	9.0	9.1	4.2	2.4	47.9	51.7	2	2
G45.804−0.356	12.0	12.3	2.8	1.3	60.0	60.0	1	1
G49.043−1.079	33.0	12.1	7.1	0.9	37.4	36.3	2	1
G49.265+0.311	7.0	6.5	1.2	1.4	–4.2	–4.6	1	2
G49.349+0.413	8.0	7.3	2.8	2.0	68.3	68.1	2	2
G49.416+0.324	8.0	9.6	0.9	0.8	–10.5	-10.2	1	1
G52.199+0.723	6.0	9.8	5.4	2.8	3.7	3.3	2	2
G52.663−1.092	4.5	5.9	2.2	2.6	65.2	65.2	1	1

Notes. Column 2 presents crude estimation of the 6.7 GHz maser peak flux density from Breen et al. (2015), Col. 3 presents peak flux densities from unpublished 6.7 GHz line survey. Data for Cols. 4 and 6 is taken from Breen et al. (2016), Table 2. Columns 5 and 7 present the same data, as in Table 1. Last two columns present number of visible features on 12 GHz spectra from Breen et al. (2016) and this survey, respectively.

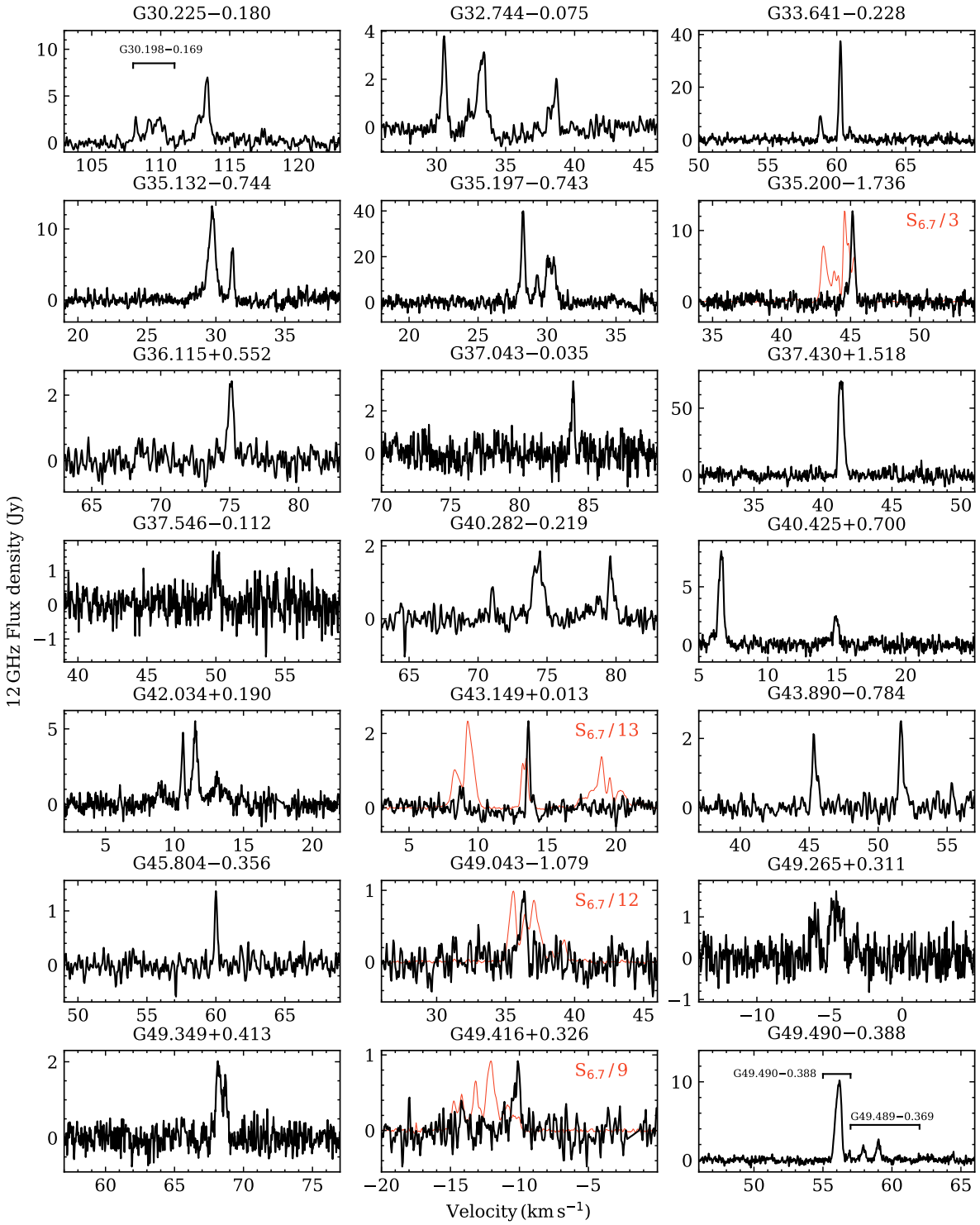

Fig. A.1. Spectra of 12.2 (black) and 6.7 GHz (red) methanol maser lines for previously known sources. The 6.7 GHz spectrum is shown only if taken contemporaneously with that at 12.2 GHz. The flux density of 6.7 GHz line is scaled by the factor given in the upper right corner.

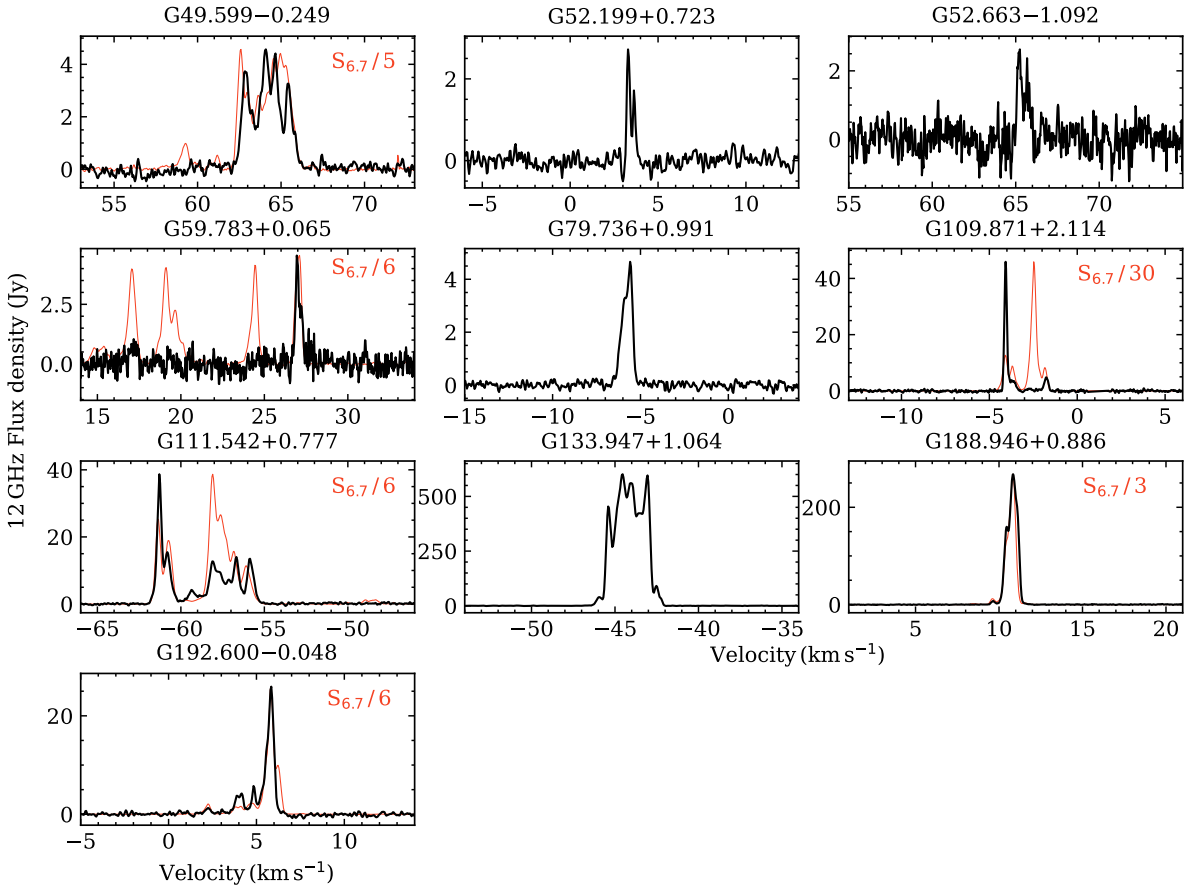

Fig. A.1. continued.